Hyperspectral Image Denoising with Fused Spatial–Spectral Smooth Operation and Graph Laplacian Regularization

Wei Lin and Shang Bao

***Abstract*—Hyperspectral images (HSIs) pose a pivotal concern in the subsequent applications. Due to the influence of optical sensing scenarios and photon effects, HSIs are always contaminated with multiple noises. This makes it challenging to accurately extract the boundaries between spatial and spectral intrinsic relations. To tackle these issues, a fused spatial-spectral smooth operation combined with graph Laplacian regularization frameworks, called FSSGLR, is proposed. The incorporation of graph Laplacian regularization endows the model with a low-rank matrix property for HSIs. Meanwhile, the fused spatial-spectral smooth operation is added to consider spatial and spectral neighborhoods simultaneously, preserving the edge information. In addition, superpixel segmentation is adopted to divide the HSIs into homogeneous regions, which showcase the superior spatial low-rank properties. The proposed FSSGLR model incorporates the Augmented Lagrange Multiplier (ALM) method to extract more discriminative spatial–spectral features. Compared to the state-of-the-art HSIs denoising methods, empirical results verify that the proposed FSSGLR yields performance comparable to or better than existing methods for HSI denoising on the Pavia Center dataset, the Toy dataset, and the real Indian Pines dataset.**

***Index Terms*—Hyperspectral images, Denoising, Fused, Smooth operation, Graph.**

I. Introduction

Over recent decades, hyperspectral imaging (HSI) has achieved significant advancements, leveraging its capacity to capture continuous spectral signatures to enable broad applications. However, noise in HSI can significantly degrade image quality and negatively impact the performance of subsequent HSI applications, such as classification [1], hyperspectral unmixing [2]. Hyperspectral images (HSIs) reflect abundant and detailed spectral information with hundreds of continuous wavebands. Subject to physical degradation from sensor aging and photon-induced effects, acquired hyperspectral images (HSIs) frequently exhibit contamination by multimodal noise—including Gaussian and impulse variants—that critically compromises data fidelity and analytical reliability. A robust denoiser for HSIs should be both effective and efficient, with strong generalizability across images from various platforms. The system should restore high-quality images when the noise pattern is known, while maintaining robust performance even under complex noise conditions. Therefore, HSI denoising has become a crucial issue for leveraging the performance and extracting discriminative information in consequent HSI applications.

Early denoising approaches often apply traditional grayscale image denoising techniques, such as BM3D [3] and NLM [4], to each band individually. Among them, HSIs can be seen simply as a 3-D cube containing many 2-D gray-scale images. However, these advanced 2-D image denoising methods overlook the potent correlations across different bands in HSIs, leading to inefficiencies and lower quality in the processed images. As a result, many HSIs denoising methods that incorporate spectral correlation have been proposed, and the low-rank (LR) prior and inter-band correlations in HSIs recovery have gained significant attention. LR-based frameworks have shown better performance in both HSIs denoising and sparse representation.

Low-rank matrix decomposition methods typically commence by unfolding HSIs into a two-dimensional matrix along the spectral dimension, subsequently applying denoising techniques to this matrix. The effectiveness of low-rank matrix decomposition stems from two key observations: it effectively captures the high spectral correlation inherent in HSIs, and it can address complex noise including impulse noise and stripe noise, all of which exhibit sparse characteristics. Then, a series of methods based on low-rank property are proposed, e.g., low-rank matrix restoration (LRMR) method [5] transforms the three-dimensional HSIs into a two-dimensional matrix by unfolding it along the spectral dimension. This approach effectively restores a clean image from the noisy HSIs. However, when employing low-rank regularization for denoising, the non-convex property of the rank function complicates the solution process. To solve this, the aforementioned LRMR framework utilizes the nuclear norm as a surrogate for the rank function. It still suffers from inefficiency under significant outliers, leading to suboptimal performance in removing mixed noise. To overcome the limitations mentioned above, spatial-spectral joint denoising methods have been developed. For example, LRTDTV [6] is based on the low-rank tensor, which leverages the global low-rank properties of HSIs. Additionally, FastHyde [8] and GLF [9] focus on spectral low-rank subspaces of HSIs. Superpixel-based methods [10], [11] divide the HSIs into superpixels with superior low-rank properties; despite their advantages in handling details, they increase computational demands.

Manuscript received February 16, 2025; revised June 15, 2025.

This work was supported in part by the Natural Science Basic Program of Shaanxi (Program No. 2025JC-YBMS-078), and the Graduate Innovation and Practical Ability Training Project of Xi'an Shiyou University (YCS23213181).

Wei Lin is an engineer of the Network and Data Center, Xi'an Shiyou University, Xi'an, Shaanxi, 710065, China (e-mail: linwei@xsyu.edu.cn).

Shang Bao is a postgraduate student of the School of Science, Xi'an Shiyou University, Xi'an, Shaanxi, 710065, China (e-mail: rickybss@163.com).

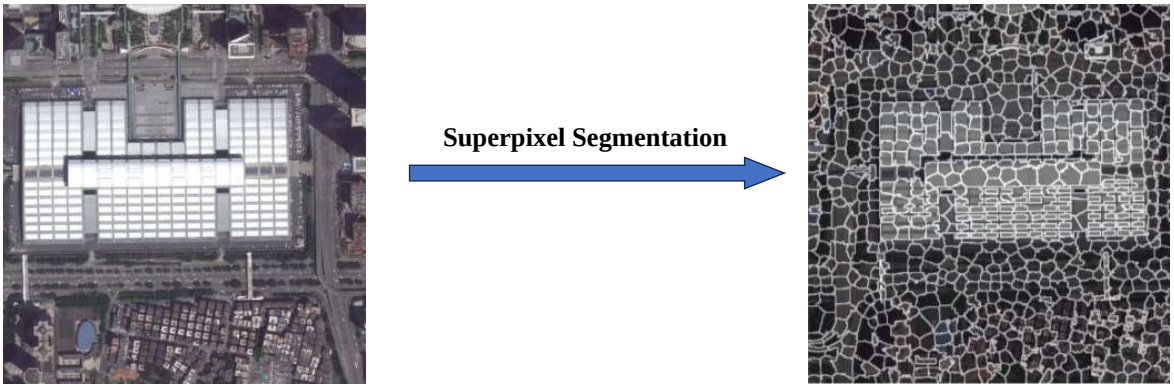

Fig. 1. Superpixel segmentation for HSI

Graph signal processing (GSP) presents an innovative methodology in signal processing by analyzing the interconnectedness of graph vertices. Graph-based regularization techniques, such as Graph Total Variation (GTV) [14] and Graph Laplacian Regularization (GLR) [15], have proven effective in HSIs denoising. Despite their strengths, graph-based methods face challenges in handling the textural details of HSIs.

To address these issues, the principal contributions of this paper in resolving these challenges are threefold:

We present the new approach that incorporates the Fused Smooth Spatial-spectral operation into Graph Laplacian Regularization for HSIs denoising model, called FSSGLR. With enhanced superior low-rank properties, a graph Laplacian model for each all-band superpixel block is adopted independently, considering each band within the superpixel block as a vertex in the graph.

We introduce fused spatial–spectral smooth operation to consider spatial and spectral neighborhoods simultaneously. The proposed optimization model is addressed through the ALM method. The proposed integrated smoothing framework effectively resolves the critical challenge of spectral-spatial discontinuity artifacts emerging in conventional denoising operations.

We carry out experiments on datasets, and empirical results show the competitive performance of our proposed FSSGLR method.

The rest of this paper is as follows, Section 2 deeply reviews relative knowledge and problem formulation. Section 3 presents the FSSGLR HSIs recovery model and derives a corresponding optimal solution using ALM. Section 4 demonstrates the superiority of the proposed FSSGLR method on Pavia center dataset, toy dataset, and real Indian dataset. Section 5 draws a conclusion and future research work.

II. Relative knowledge and problem formulation

A. Superpixel Segmentation for HSIs

Homogeneous local regions demonstrate a stronger low-rank property compared to rectangular blocks, as shown in [11]. To capture these regions, superpixel segmentation is applied to partition the HSIs into regions with adaptive sizes and shapes, known as superpixels, which inherently share similarities.

Superpixel segmentation is typically used for 2-D images. In our study, prior to applying superpixel segmentation to the HSIs, each spectral band is regarded as a 2-D grayscale image. Information entropy [16] is employed to evaluate the image quality across all bands, serving as an indicator of noise impact. Higher information entropy values signify better image quality. Consequently, following the Simple Linear Iterative Clustering (SLIC) methodology [17], the spectral band exhibiting maximum entropy is prioritized for superpixel segmentation. The segmentation results are then applied to all bands of the HSIs. The entire segmentation procedure is depicted in Fig. 1.

B. Graph Representation for Superpixel Blocks

Given $x \in R^n$, we denote an undirected weighted graph $\mathcal{G}$. Let $\mathcal{G} = (V, E, \mathbf{W})$, where $\mathcal{V} = \{v_1, ..., v_N\}$ with vertex $v_i, i = 1, 2, \cdots, n$, and $\mathcal{E}$ represents the set of edges. The adjacency matrix $\mathbf{W} = (w_{ij}) \in R^{N\times N}$ with its non-negative weight entry w_{ij} is computed as follows:

$$w_{ij} = \begin{cases} 0, & \text{if } v_i \text{ is not in the k-neighborhood of } v_j \\ \exp\left(-\frac{\text{dist}(v_i,v_j)}{\sigma_v}\right), & \text{otherwise.} \end{cases} \tag{1}$$

where $\text{dist}(v_i, v_j)$ represents the Euclidean distance between vertex v_i and v_j nodes in R^N, σ_v is a scalar parameter in the heat kernel computation [18].

The graph Laplacian matrix is denoted as

$$\mathbf{L} := \mathbf{D} - \mathbf{W}, \tag{2}$$

where $\mathbf{D}$ is the diagonal matrix of node degrees, given by $\text{diag}(d_1, \ldots, d_N)$, and each diagonal entry d_i satisfies with diagonal elements $d_i = \sum_{j=1}^{N} w_{ij}$.

Given a set of signals $s_1, s_2, \cdots, s_N$ corresponding to the signal values of vertices $v_1, v_2..., v_N$ in the graph $\mathcal{G}$, we denote $S_\mathcal{G} = \sum_{i=1}^{N} s(v_i)$ as the graph signal.

Let $a_\mathbf{i} \in R^{Q\times 1}$ be the vector representing the $\mathbf{i}$-th superpixel with Q pixels. B represents the number of bands in the HSIs. The 2-D matrix unfolding in dictionary order of an all-band superpixel block is denoted as$\mathbf{A_i} \in R^{Q\times B}$. Each all-band superpixel block is treated as an independent graph, with graph vertices corresponding to superpixels in each band.

The graph signal $S_\mathcal{G}$ [15] of GLR can be formulated as:

$$\|S_{\mathcal{G}}\|_{\mathrm{GLR}}=\frac{1}{2}\sum_{i=1}^{N}\sum_{j=1}^{N}w_{i,j}\parallel s(v_i)-s(v_j)\parallel_2^2=\mathrm{Tr}\big(S_{\mathcal{G}}\mathbf{L}S_{\mathcal{G}}^T\big), \tag{3}$$

where $\mathrm{Tr}(\cdot)$ denotes the matrix trace operator.

To ensure the smoothness between graph signals, the GLR is commonly introduced into the model. Moreover, [21] demonstrates that, compared to the nuclear norm, GLR can more efficiently constrain the low-rank properties of matrices while also saving significant computational resources.

C. Degradation Model of HSIs

Real-world collected HSI contains multiple types of noise. The observed HSIs under normal circumstances $\mathcal{O}$ can be expressed as a combination of three components: the clean HSIs $\mathcal{X}$, sparse noise $\mathcal{S}$, and Gaussian noise $\mathcal{N}$. The degradation model is formulated as:

$$\mathcal{O}=\mathcal{X}+\mathcal{S}+\mathcal{N}, \tag{4}$$

where $\mathcal{O},\mathcal{X},\mathcal{S},\mathcal{N}$ are matrices with dimensions $M\times N\times B$, with M and N representing the spatial dimensions of the HSIs, and B representing the number of spectral bands.

To facilitate processing, the HSIs $\mathcal{O}$ is segmented into K superpixel blocks using the SLIC algorithm. For the i-th superpixel block, $\mathcal{O}_i,\mathcal{X}_i,\mathcal{S}_i$ are the observed HSIs, clean HSIs, and sparse noise, respectively. These components are reshaped into 2D matrices $\mathbf{O}_i,\mathbf{X}_i,\mathbf{S}_i$, respectively. We propose a unified denoising framework to restore the clean HSI $\mathcal{X}$ from its noise-corrupted observation HSIs $\mathcal{O}$.

III. Proposed method

In this section, we introduce the proposed FSSGLR model, and tackle the proposed optimization model by employing ALM.

By incorporating the Fused Spatial–spectral Smooth operation into the Graph Laplacian Regularization model with superpixel segmentation [19], we obtain a new model for HSI denoising, called FSSGLR. The proposed model is

$$\min_{\mathbf{X},\mathbf{S},\mathbf{Z}}\sum_{i=1}^{K}\left(\|\mathbf{X}_i\|_{\mathrm{GLR}}+\alpha\|\mathbf{S}_i\|_1+\beta\|\mathbf{Z}\|_1\right) \tag{5}$$

$$\text{s.t.}\quad \|\mathbf{O}_i-\mathbf{X}_i-\mathbf{S}_i\|_F^2\le\zeta,\quad \mathbf{Z}=\mathrm{Smooth}(\mathbf{X}),$$

where:

- $\|\mathbf{X}_i\|_{\mathrm{GLR}}$ is the graph Laplacian regularization with $\mathbf{X}_i$ for the i-th superpixel block.
- $\|\mathbf{S}_i\|_1$ and $\|\mathbf{Z}\|_1$ represent the ℓ_1-norms for sparse noise and the fused spatial-spectral smooth operator, respectively.
- α and β are two nonnegative regularization terms.
- ζ is the tolerance for the reconstruction error.

A. Optimization Model

Equivalently, the overall optimization problem is formulated as:

$$\min_{\mathbf{X},\mathbf{S},\mathbf{Z}}\sum_{i=1}^{K}\left(\mathrm{Tr}(\mathbf{X}_i\mathbf{L}_i\mathbf{X}_i^T)+\alpha\|\mathbf{S}_i\|_1+\beta\|\mathbf{Z}\|_1\right), \tag{6}$$

$$\text{s.t.}\quad \|\mathbf{O}_i-\mathbf{X}_i-\mathbf{S}_i\|_F^2\le\zeta,\quad \mathbf{Z}=\mathrm{Smooth}(\mathbf{X}),$$

where $\mathrm{Tr}(\mathbf{X}_i\mathbf{L}_i\mathbf{X}_i^T)$ is the matrix trace, with $\mathbf{L}_i$ being the Laplacian matrix for the i-th superpixel block.

The smooth operator $\mathrm{Smooth}(\mathbf{X})$ is defined as:

$$\mathrm{Smooth}(\mathbf{X})=\mathrm{Smooth}_{\text{spectral}}(\mathrm{Smooth}_{\text{space}}(\mathbf{X})). \tag{7}$$

where:

- **Spatial smoothing**

$$\mathrm{Smooth}_{\text{space}}(\mathbf{X})_{i,j,b}=\begin{cases}\frac{1}{|N(i,j)|}\sum_{(k,l)\in N(i,j)}\mathbf{X}_{k,l,b}, & (i,j)\in\text{boundary},\\ \mathbf{X}_{i,j,b}, & \text{otherwise.}\end{cases} \tag{8}$$

where spatial smooth operation is determined by the average of $\mathbf{X}_{k,l,b}$ if (k,l) belongs to neighborhood of boundary (i,j) under fixed band b.

- **Spectral smoothing**

$$\mathrm{Smooth}_{\text{spectral}}(\mathbf{X})_{i,j,b}=\begin{cases}\frac{1}{3}\sum_{k=-1}^{1}\mathbf{X}_{i,j,b+k}, & b\in\{2,\dots,B-1\},\\ \mathbf{X}_{i,j,b}, & b=1\text{ or }B.\end{cases} \tag{9}$$

where spectral smooth operation $\mathrm{Smooth}_{\text{spectral}}(\mathbf{X})_{i,j,b}$ is the average sum of $\mathbf{X}_{i,j,b-1},\mathbf{X}_{i,j,b}$, and $\mathbf{X}_{i,j,b+1}$ if the band is neither 1 nor B.

B. Optimization Procedure

The optimization model is addressed through the **ALM** method. The augmented Lagrangian function is expressed as:

$$\begin{aligned}&\mathcal{L}(\mathbf{X},\mathbf{S},\mathbf{Z},\mathbf{Y}^X,\mathbf{Y}^Z,\rho)\\&=\sum_{i=1}^{K}\left(\mathrm{Tr}(\mathbf{X}_i\mathbf{L}_i\mathbf{X}_i^T)+\alpha\|\mathbf{S}_i\|_1+\beta\|\mathbf{Z}\|_1\right)\\&+(\mathbf{Y}_i^X)^T(\mathbf{O}_i-\mathbf{X}_i-\mathbf{S}_i)\quad+\frac{\rho}{2}\|\mathbf{O}_i-\mathbf{X}_i-\mathbf{S}_i\|_F^2\\&+(\mathbf{Y}^Z)^T(\mathbf{Z}-\mathrm{Smooth}(\mathbf{X}))\quad+\frac{\rho}{2}\|\mathbf{Z}-\mathrm{Smooth}(\mathbf{X})\|_F^2.\end{aligned} \tag{10}$$

Alternatively, we can decompose problem (10) into four sub-problems and optimize the variables sequentially, while fixing the other variables when solving each subproblem. Consequently, the variables in problem (10) are obtained in the following manner at the $(t+1)$th iteration :

1. Update $\mathbf{X}_i$

$$\begin{aligned}\mathbf{X}_i^{t+1}=\arg\min_{\mathbf{X}_i}&\mathrm{Tr}(\mathbf{X}_i\mathbf{L}_i\mathbf{X}_i^T)\\&+\frac{\rho}{2}\|\mathbf{O}_i-\mathbf{X}_i-\mathbf{S}_i^t+\frac{\mathbf{Y}_i^X}{\rho}\|_F^2\\&+\frac{\rho}{2}\|\mathbf{Z}^t-\mathrm{Smooth}(\mathbf{X}_i)+\frac{\mathbf{Y}^Z}{\rho}\|_F^2.\end{aligned} \tag{11}$$

2. Update $\mathbf{S}_i$

$$\mathbf{S}_i^{t+1}=\arg\min_{\mathbf{S}_i}\alpha\|\mathbf{S}_i\|_1+\frac{\rho}{2}\|\mathbf{O}_i-\mathbf{X}_i^{t+1}-\mathbf{S}_i+\frac{\mathbf{Y}_i^X}{\rho}\|_F^2. \tag{12}$$

The solution is given by the soft-thresholding operator:

$$\mathbf{S}_i^{t+1}=\mathrm{shrink}_{\ell_1}\left(\mathbf{O}_i-\mathbf{X}_i^{t+1}+\frac{\mathbf{Y}_i^X}{\rho},\frac{\alpha}{\rho}\right). \tag{13}$$

3. Update $\mathbf{Z}$

$$\mathbf{Z}^{t+1} = \arg\min_{\mathbf{Z}} \beta\|\mathbf{Z}\|_1 + \frac{\rho}{2}\|\mathbf{Z} - \text{Smooth}(\mathbf{X}^{t+1}) + \frac{\mathbf{Y}^Z}{\rho}\|_F^2. \tag{14}$$

The solution is:

$$\mathbf{Z}^{t+1} = \text{shrink}_{\ell_1}\left(\text{Smooth}(\mathbf{X}^{t+1}) + \frac{\mathbf{Y}^Z}{\rho}, \frac{\beta}{\rho}\right). \tag{15}$$

4. Update Lagrange Multiplier

$$\mathbf{Y}_i^{X,t+1} = \mathbf{Y}_i^X + \rho(\mathbf{O}_i - \mathbf{X}_i^{t+1} - \mathbf{S}_i^{t+1}), \tag{16}$$

$$\mathbf{Y}^{Z,t+1} = \mathbf{Y}^Z + \rho(\mathbf{Z}^{t+1} - \text{Smooth}(\mathbf{X}^{t+1})). \tag{17}$$

5. Iteration stopping condition

The stopping criterion $\zeta = 10^{-6}$ and maximum iteration $\tau = 50$.

The proposed method is summarized in Algorithm 1.

Algorithm 1 FSSGLR

1: **Input**: The observed HSI $\mathbf{O}$, rank r, the number of superpixels K, parameters $\alpha = 0.01$ and $\beta = 0.2$, the stopping criterion $\zeta = 10^{-6}$ and maximum iteration $\tau = 50$
2: **Output**: Desired clean HSI $\mathbf{X}$
3: **Initialization**:
- Set $\mathbf{O} = \mathbf{X_i}$; $\mathbf{S_i} = \mathbf{0}$; $\mathbf{Z} = \mathbf{X}$
- Select the band with the highest quality for the superpixel segmentation, apply to all bands and construct the graph.

4: **for** $i = 1, 2, \cdots, K$ **do**
5: **while** $\tau \leq 50$ **do**
6: Update $\mathbf{X}_i$, $\mathbf{S}_i$ and $\mathbf{Z}$ via (11), (12) and (14) respectively;
7: Update $\mathbf{Y}_i^X, \mathbf{Y}^Z$ by (16) and (17), respectively;
8: Check the conditions for stopping the iteration:
9: $\|\mathbf{O}_i - \mathbf{X}_i - \mathbf{S}_i\|_F^2 \leq \zeta$,
10: **end while**
11: **end for**

IV. Experiments

In this section, experiments are set up on simulated Pavia center and toy datasets, and real Indian datasets in order to verify the efficacy of the proposed method (FSSGLR) in the removal of HSIs mixed noise. Different types of HSIs denoising existing methods are selected for comparison in the simulation experiments, including BM4D [20], LRMR [5], LRTDTV [6], FastHyDe [8], GLF [9] and FGLR [21]. All experiments are based on MATLAB (2016a) with Intel Core I7-8750H 2.2GHz CPU and 16GB RAM.

A. Evaluation Metrics

There are four quantitative quality indices in the simulation experiments. These are MPSNR, MSSIM, ERGAS, and MSAM, respectively. To evaluate the overall recovery quality of HSIs, we use MPSNR and MSSIM. Moreover, ERGAS is a spectral-based evaluation measure, while MSAM provides an additional assessment of spectral accuracy.

$$\text{MPSNR} = \frac{1}{B}\sum_{b=1}^{B} 10\log_{10}\frac{\max(\text{X}(:,:,b))^2}{\|\text{X}(:,:,b) - \widehat{\text{X}}(:,:,b)\|_F^2} \tag{18}$$

where $\max(\text{A})$ returns the largest element in matrix A. Symbols $\text{X}(:,:,b)$ and $\widehat{\text{X}}(:,:,b)$ represent the clean b-th band and the estimated b-th band, respectively.

$$\text{MSSIM} = \frac{1}{B}\sum_{b=1}^{B} \text{SSIM}(\text{X}(:,:,b), \widehat{\text{X}}(:,:,b)) \tag{19}$$

where the Structural Similarity Index Measure (SSIM) quantifies the perceptual similarity between images $\mathbf{A}$ and $\mathbf{B}$ through:

$$\text{SSIM}(\mathbf{A}, \mathbf{B}) \in [-1, 1]$$

When values approaching 1 indicate higher structural resemblance. This metric emulates the human visual system (HVS) by jointly evaluating luminance, contrast, and structural patterns, making it more consistent with subjective image quality assessment than traditional pixel-wise metrics.

ERGAS (Relative Global Error Synthesis) quantifies reconstruction fidelity in multispectral data, where values approaching zero indicate superior spectral and spatial accuracy. The ERGAS is denoted by

$$\text{ERGAS} = \sqrt{\frac{1}{p}\sum_{i=1}^{p}\frac{\text{mse}(u_i, \hat{u}_i)}{\text{Mean}_2(u_i)}} \tag{20}$$

where $\text{mse}(\cdot,\cdot)$ denotes the MSE performance function and $\text{Mean}_2(\cdot)$ is the mean of the matrix elements.

This metric accounts for inter-band variability by normalizing each band's MSE against its mean intensity, ensuring balanced sensitivity across diverse brightness levels. By holistically integrating normalized errors, it aligns more closely with perceptual quality in remote sensing applications than isolated pixel-wise measures.

Lastly, the Mean Spectral Angle Mapper (MSAM) is calculated as follows:

$$\text{MSAM} = \frac{1}{N}\sum_{i=1}^{N}\arccos\left(\frac{\sum_{j=1}^{n}(r_{ij} - m_{ij})}{\sqrt{\sum_{j=1}^{n}(r_{ij} - \bar{r}_j)^2}\cdot\sqrt{\sum_{j=1}^{n}(m_{ij} - \bar{m}_j)^2}}\right) \tag{21}$$

where r_j and m_j represent the j-th values of the reference and target spectral, respectively, with n being the length of the spectral data, and $\bar{r}_j$ and $\bar{m}_j$ denoting their mean values.

The results of HSIs are considered better when the MPSNR and MSSIM values are higher, while the ERGAS and MSAM values are smaller.

Table I Parameter Selection of Experiment for Four Different Simulation Cases

case \ parameter	$\boldsymbol{\sigma}$	P	m
Case 1	0.05	0.05	0
Case 2	0.1	0.05	0
Case 3	0.05	0.05	0.3
Case 4	0.1	0.05	0.5

Table II QUANTITATIVE EVALUATION OF SELECTED METHODS FOR THE PAVIA CENTER DATASET

Case	Index	Noisy	BM4D	LRMR	LRTDTV	FastHyDe	GLF	FGLR	Ours
Case 1	MPSNR	16.613	18.657	33.323	30.096	31.149	31.272	35.401	**36.284**
	MSSIM	0.295	0.410	0.890	0.837	0.891	0.895	**0.938**	0.891
	ERGAS	686.716	544.768	101.212	147.799	130.136	127.346	**80.563**	90.141
	MSAM	0.434	0.351	0.085	0.085	0.073	**0.071**	**0.071**	0.101
Case 2	MPSNR	14.648	15.733	29.506	27.221	27.849	27.964	33.315	**34.134**
	MSSIM	0.186	0.226	0.797	0.772	0.836	0.840	**0.898**	0.831
	ERGAS	868.310	767.508	158.078	213.890	194.362	190.901	**99.930**	113.894
	MSAM	0.460	0.428	0.112	0.104	0.091	0.089	**0.086**	0.113
Case 3	MPSNR	16.419	18.337	30.794	28.052	28.869	28.920	32.604	**33.306**
	MSSIM	0.288	0.397	0.863	0.812	0.862	0.866	**0.915**	0.960
	ERGAS	704.446	567.797	162.289	205.377	201.102	197.843	134.670	**128.772**
	MSAM	0.398	0.339	0.110	**0.103**	0.105	**0.103**	0.114	0.106
Case 4	MPSNR	14.529	15.562	27.124	25.182	25.784	25.791	30.324	**30.502**
	MSSIM	0.181	0.219	0.765	0.749	0.805	0.807	**0.865**	0.786
	ERGAS	875.101	776.954	234.949	278.020	278.041	275.565	171.921	**165.020**
	MSAM	0.438	0.406	0.139	0.121	0.126	0.124	0.141	**0.113**

Table III QUANTITATIVE EVALUATION OF SELECTED METHODS FOR THE TOY DATASET

Case	Index	Noisy	BM4D	LRMR	LRTDTV	FastHyDe	GLF	FGLR	Ours
Case 1	MPSNR	16.363	18.207	26.781	28.755	29.530	29.764	29.651	**31.381**
	MSSIM	0.198	0.295	0.509	0.628	0.695	0.689	0.722	**0.783**
	ERGAS	631.323	510.848	190.364	152.022	139.047	**134.870**	205.631	197.559
	MSAM	1.511	1.230	0.833	0.530	0.530	**0.455**	1.050	0.588
Case 2	MPSNR	15.586	17.125	24.653	26.055	26.587	26.666	27.480	**28.075**
	MSSIM	0.128	0.180	0.377	0.556	**0.624**	0.617	0.570	0.583
	ERGAS	690.204	578.216	242.806	207.158	194.450	**192.642**	225.375	225.454
	MSAM	1.569	1.344	0.840	0.528	0.537	**0.490**	0.905	0.611
Case 3	MPSNR	16.154	17.949	25.725	26.896	27.338	27.775	28.194	**29.794**
	MSSIM	0.187	0.274	0.475	0.581	0.643	0.650	0.663	**0.694**
	ERGAS	646.732	526.402	227.085	197.586	194.282	**189.416**	230.551	215.188
	MSAM	1.439	1.222	0.837	0.568	0.567	0.577	1.015	**0.552**
Case 4	MPSNR	15.180	18.310	23.653	24.114	24.475	25.978	25.132	**26.576**
	MSSIM	0.120	0.235	0.460	0.453	0.456	**0.555**	0.512	0.526
	ERGAS	725.911	542.699	358.124	298.451	311.553	253.077	265.736	**239.767**
	MSAM	1.441	1.407	1.218	0.859	0.926	0.727	0.825	**0.570**

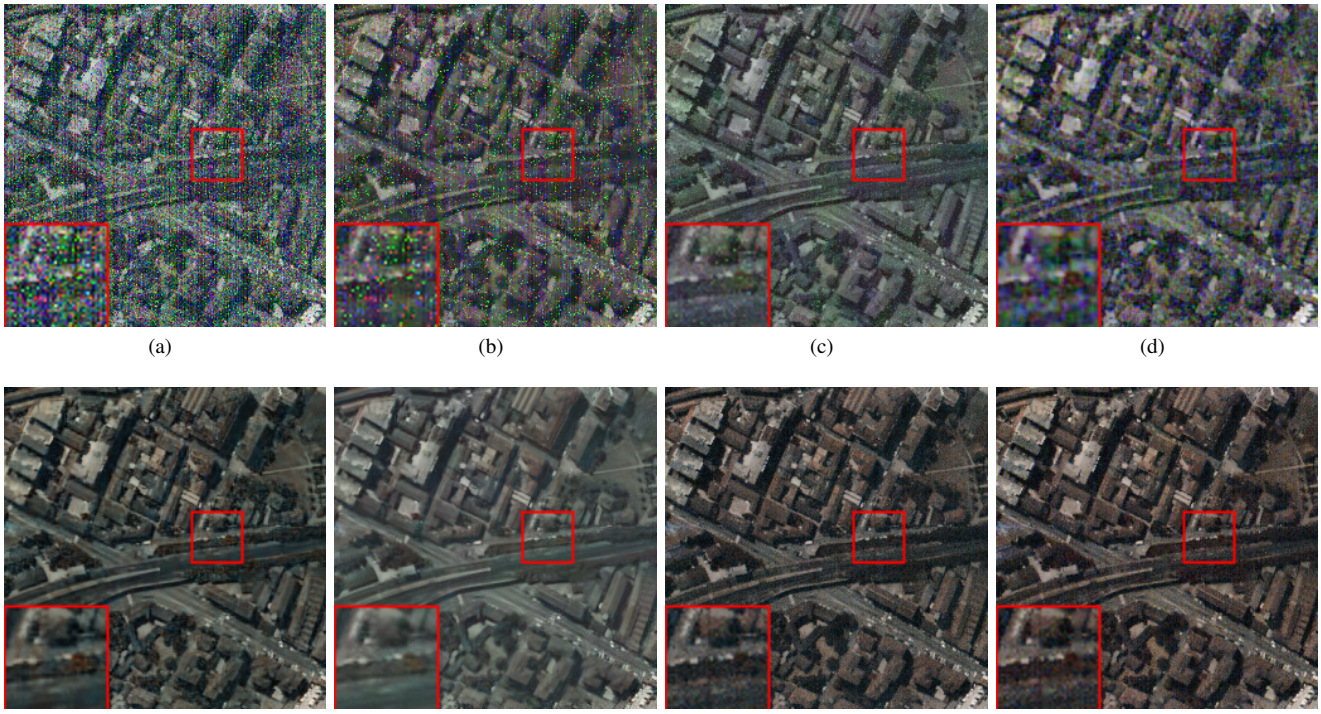

(a) (b) (c) (d)

(e) (f) (g) (h)

Fig. 2. Denoising results for simulated Pavia center dataset. (a) Noisy HSI, (b) BM4D, (c) LRMR, (d) LRTDTV, (e) FastHyDe, (f) GLF, (g) FGLR, (h) Ours.

(a) (b) (c) (d)

(e) (f) (g) (h)

Fig. 3. Denoising results for simulated toy dataset. (a) Noisy HSI, (b) BM4D, (c) LRMR, (d) LRTDTV, (e) FastHyDe, (f) GLF, (g) FGLR, (h) Ours.

B. Simulated Data Experiments

For the convenience of simulated experiments, Pavia Center and Toy datasets are selected, from which we have extracted smaller samples sized 256 × 256 × 80 and 200 × 200 × 100, respectively. All datasets are normalized to [0,1] band by band. In these experiments, mixed noises are introduced in the clean data, including Gaussian noise, impulse noise, and stripe noise with different intensities, to simulate the observed HSIs.

Let σ represent the standard deviation associated with the Gaussian noise, and suppose that P indicates the proportion of impulse noise present. In addition, m denotes the percentage of bands contaminated by $[10, 30]$ stripe noise. Parameter selection of four different cases is introduced to simulated experiments in Table I. The noise distribution differs between bands in all datasets, with stripe noise-contaminated bands and columns randomized in their selection.

Table II compares the denoising results of selected hyperspectral image denoising methods for the Pavia center dataset. Through this comparative analysis, it can be concluded that our FSSGLR demonstrates significant advantages in the task of HSIs denoising. In terms of performance across various metrics, FSSGLR ranks second to the FGLR method in terms of three metrics on Case 1 and Case 2, where GLF is slightly suboptimal. However, on Case 3 and Case 4, FSSGLR achieves the best performance. Regarding other evaluation metrics such as mean structural similarity (MSSIM), global relative error (ERGAS), and mean spectral angular mapping (MSAM), FSSGLR consistently delivers optimal results across all four cases. Therefore, it can be inferred that FSSGLR exhibits strong robustness in effectively removing mixed noise from HSIs.

As shown in Table III, the proposed method consistently outperforms all other algorithms, achieving the highest MPSNR values across all scenarios. In contrast, the FGLR algorithm proves less effective, underperforming in most of the bands. Remarkably, both the proposed method and FGLR, which are grounded in graph Laplace normalization regularization, demonstrate more stable and consistent performance across waveband variations when compared to competing methods. This not only validates the effectiveness of the proposed FSSGLR but also underscores the superior capability of graph signal processing techniques in ensuring smooth, reliable performance for high-dimensional data.

The visualization in Fig. 2 presents the synthesized results from the Pavia Center dataset on Case 4. From the analysis, the denoising results of the BM4D method are still significantly contaminated by noise. While LRMR and LRTDTV show some visual improvement, noticeable noise remains. In the denoising results of FastHyDe, a small amount of stripe noise is evident, indicating that the method is not robust in removing stripe artifacts. The GLF method shows substantial visual improvement, but localized blurring issues still persist. The FGLR method, on the other hand, lacks sufficient detail and texture preservation in certain areas, while the proposed method effectively addresses these issues, providing excellent texture preservation and superior visual quality.

Fig. 3 illustrates the denoising results for the toy dataset on Case 4. Toy dataset has vivid colors and rich details. Although the LRMR method removes some Gaussian noise, a significant amount of stripe noise remains. The FGLR method performs well in removing stripe noise but still exhibits Gaussian and impulse noise in localized areas. LRTDTV and GLF suffer from over-smoothing, which leads to blurred details. FastHyDe shows visual improvement on Case 4, but impulse noise persists in the locally enlarged regions. Meanwhile, the proposed FSSGLR effectively addresses these issues in both the global and locally enlarged regions, resulting in visually promising performance compared to other methods.

Fig. 4 and Fig. 5 show the curves of PSNR and SSIM as they vary with the bands for each algorithm under simulated Pavia center and toy datasets, respectively. From Fig. 4(a) and Fig. 5(a), the proposed FSSGLR algorithm achieves the highest PSNR values in most bands, while the FGLR algorithm performs as the sub-optimal in most bands. Compared to other methods, these two algorithms based on graph Laplacian regularization exhibit more stable performance across different bands. This result not only validates the effectiveness of the FSSGLR method proposed but also demonstrates the superiority of graph signal processing methods in handling the smoothness of high-dimensional data. At the same time, from Fig. 4(b) and Fig. 5(b), the proposed FSSGLR yields superior SSIM values in almost all bands, as clearly seen in the visual results, further proving its advantage in preserving structure. Based on the results from Fig. 4 and 5, it can be concluded that FSSGLR has a significant advantage, especially in spatial dimension denoising, under low-noise conditions.

C. Ablation Experiments

This subsection conducts an ablation study to evaluate the contribution of each module in the FSSGLR algorithm. Specifically, the noisy module represents the raw, untreated data of the Pavia center dataset. The second module applies nuclear norm constraints while also incorporating norm-based sparse noise component constraints. The third module, based on the second one, replaces the nuclear norm constraint with the GLR constraint proposed, and the FSSGLR module represents the complete algorithm proposed in this paper. The results of the ablation study are shown in Table IV.

According to the results in the Table IV, it can be seen that using the core norms $\|\cdot\|$ and ℓ_1-norm can effectively remove high-frequency noise in HSIs, but the results are still not ideal. On this basis, by using image deblurring regularization, the core norm $\|\cdot\|_{\mathrm{GLR}}$ significantly improves the MPSNR by 1.887 dB, with other indicators also showing clear improvement. Meanwhile, the FSSGLR algorithm shows a substantial improvement in both models, with the MPSNR values increasing by 2.923 dB and 1.036 dB, respectively. The denoising effect has been significantly enhanced. Therefore, experimental results verify that the FSSGLR method has advantages in local error control and preserving image fidelity, fully demonstrating the effectiveness of each calculation module.

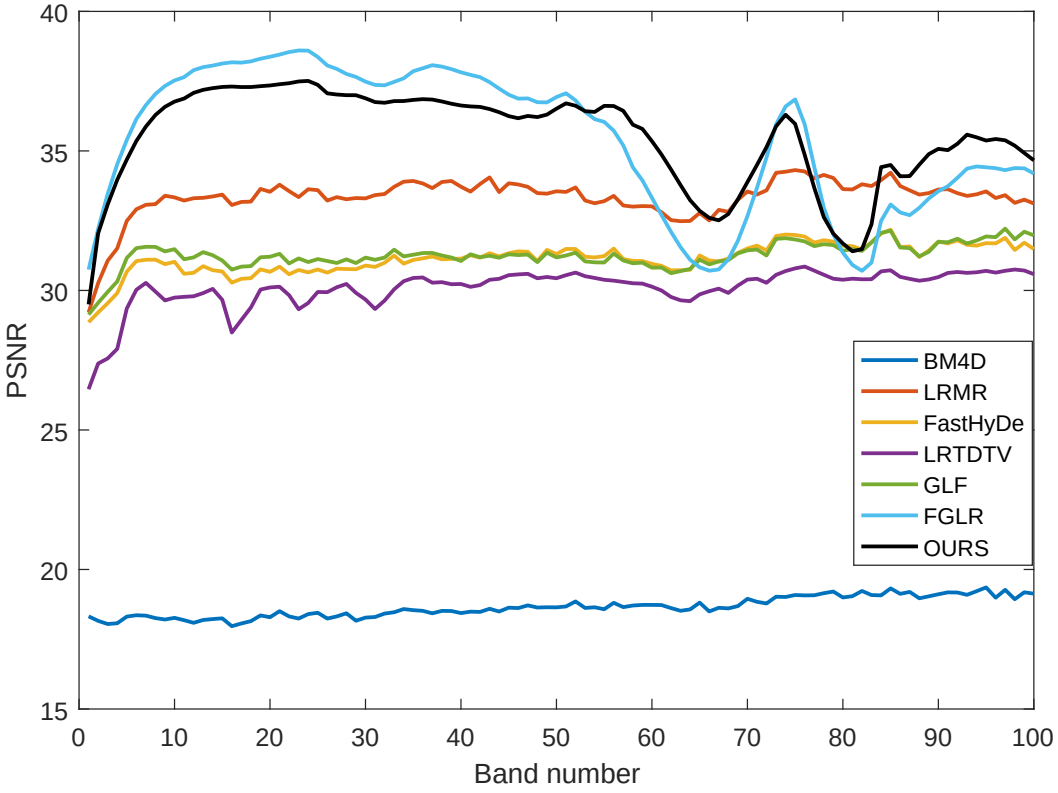

(a)

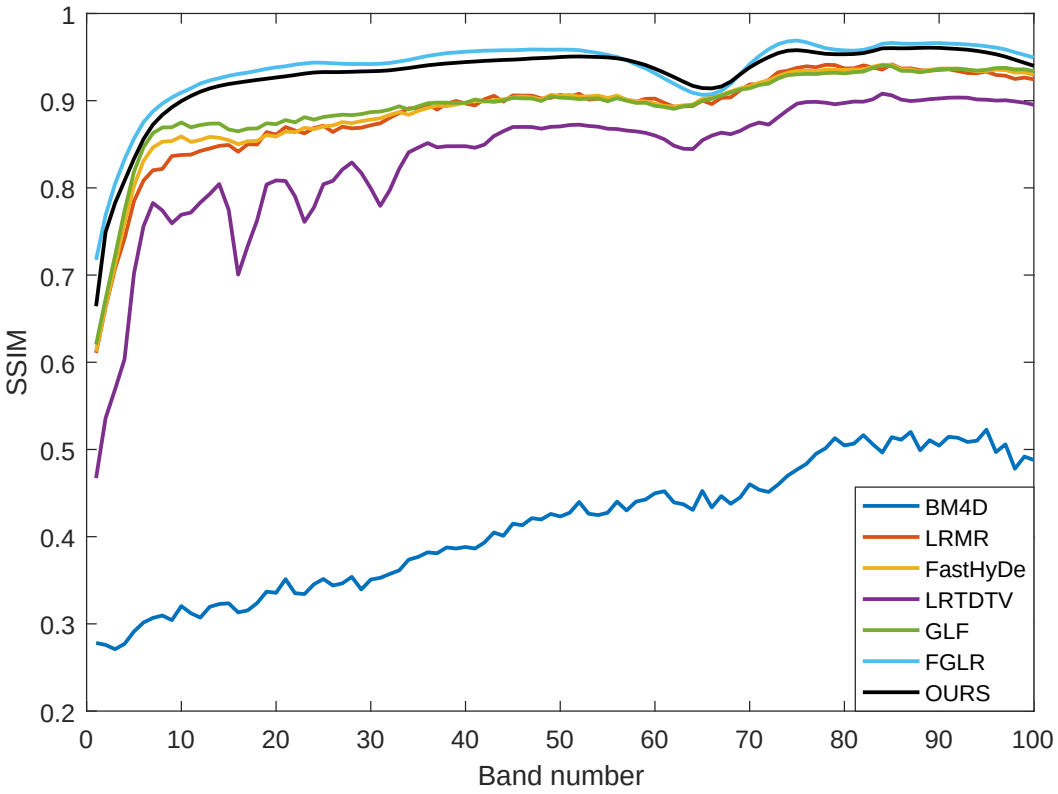

(b)

Fig. 4. The (a) PSNR and (b) SSIM values for different algorithms of the simulated Pavia dataset on Case 1.

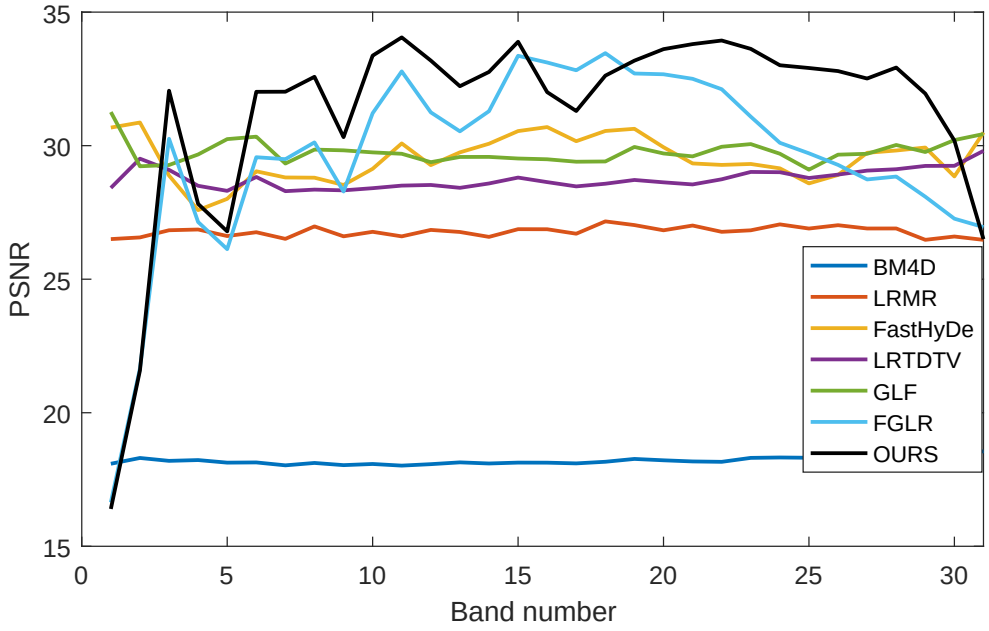

(a)

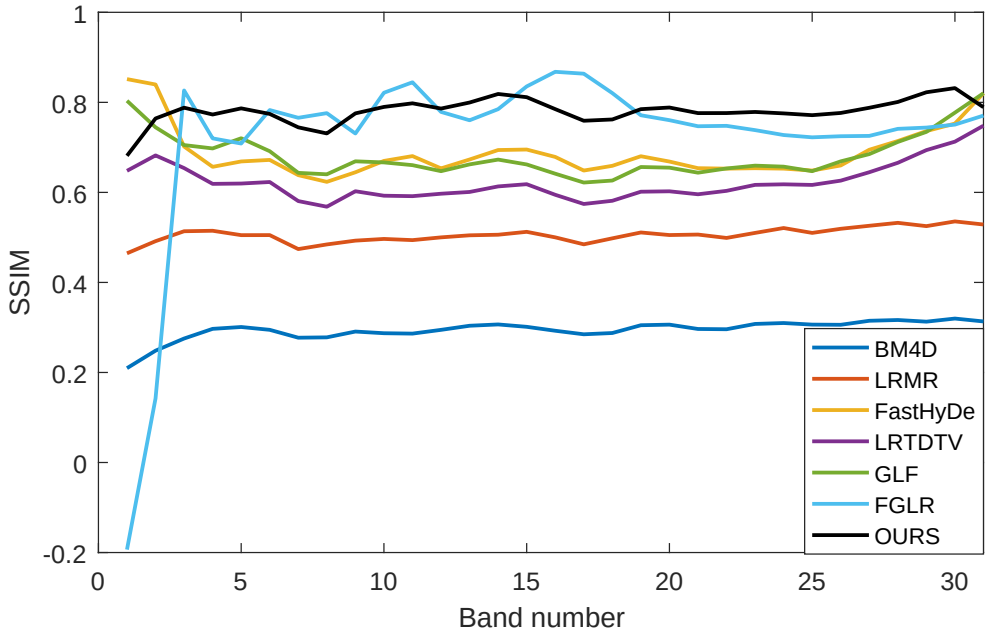

(b)

Fig. 5. The (a) PSNR and (b) SSIM values for different algorithms of the toy dataset on Case 1.

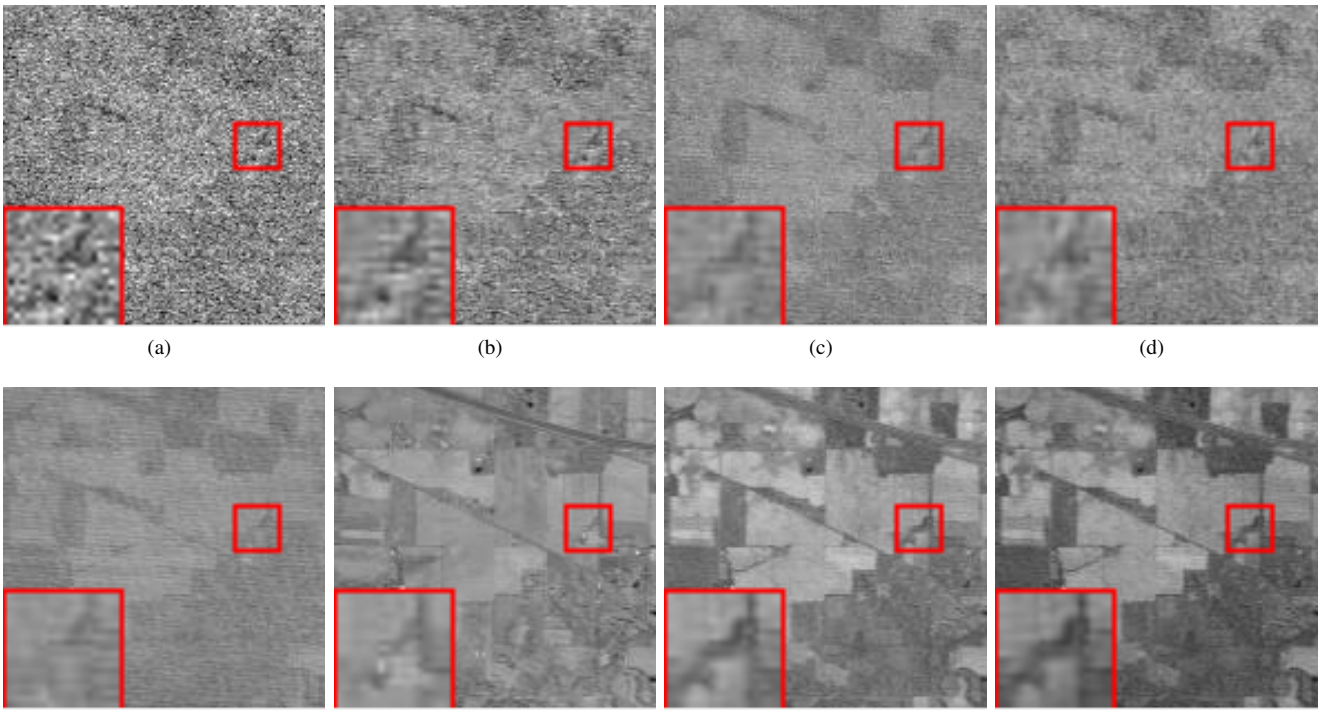

Fig. 6. Denoising results for real Indian dataset. (a) Noisy HSI, (b) BM4D, (c) LRMR, (d) LRTDTV, (e) FastHyDe, (f) GLF, (g) FGLR, (h) Ours.

Table IV
ABLATION STUDY OF FSSGLR

MODULES	MPSNR	MSSIM	ERGAS	MSAM
Noisy	15.180	0.120	725.911	1.441
$\|\mathbf{X}\|_* + \|\mathbf{S}\|_1$	23.653	0.460	298.451	1.218
$\|\mathbf{X}\|_{\mathrm{GLR}} + \|\mathbf{S}\|_1$	25.540	0.501	279.716	0.572
FSSGLR	**26.576**	**0.526**	**239.767**	**0.570**

D. Real Datasets Experiments

Real Indian dataset experiments are conducted to show the effectiveness of the proposed FSSGLR in practical applications. The Indian Pines dataset (145 × 145 × 220), contaminated with severe mixed noise in some bands, is selected for evaluation. Visual results of various denoising methods are presented in Fig. 6. Comparing the global and zoomed-in images reveals that BM4D, LRMR, and LRTDTV remain heavily affected by noise. FastHyde and GLF exhibit some noise contamination, though the overall features of the HSIs are discernible. FGLR struggles to capture textural details effectively. In comparison, the proposed method exhibits superior performance in this experiment.

The running time of the different methods on the real Indian dataset is detailed in Table V. From Table V, the proposed method on the real Indian dataset cost a longer time than FastHyDe and GLR.

Table V
RUNNING TIME ON REAL INDIAN DATASET

Index	BM4D	LRMR	LRTDTV	FastHyDe	GLF	FGLR	FSSGLR
Time(s)	153.208	77.295	20.114	2.995	303.406	4.210	9.143

E. Datasets Supplementary Information

- Pavia center dataset: The Pavia center dataset is collected from aerial imagery by the University of Pavia. It features multiple spectral bands, each representing a specific wavelength.
- Toy dataset: The toy datasets include the Iris, Diabetes, Digits, Linnerud, Wine, and Breast Cancer datasets. These datasets are synthetic and designed for experimental purposes, consisting of small-scale data with simple patterns. They contain tens to hundreds of samples, allowing for controlled experimentation.
- Real Indian dataset: The real Indian dataset encompasses diverse, real-world data sourced from India, potentially including hyperspectral remote sensing, agricultural observations, or socioeconomic statistics, characterized by geographic and cultural specificity.

V. Conclusion

In this paper, we propose an effective HSIs denoising method, namely FSSGLR, which incorporates a fused smooth spatial-spectral operation into a GLR-based model, yielding better performance in certain bands. Synthetic and real datasets validate that the proposed FSSGLR method is superior compared with the existing HSIs denoising methods. Further work needs to be done to investigate the runtime of the proposed method and optimization approaches to tackle the challenge of HSIs denoising.

References

[1] Xiangyong Cao, Feng Zhou, Lin Xu, Deyu Meng, Zongben Xu and John Paisley, “Hyperspectral image classification with Markov

random fields and a convolutional neural network," IEEE Transactions on Image Processing, vol. 27, no. 5, pp2354–2367, 2018

[2] Chenguang Xu, "Adaptive total variation regularization for weighted low-rank tensor sparse hyperspectral unmixing," IAENG International Journal of Applied Mathematics, vol. 54, no. 11, pp2404–2417, 2024

[3] Kostadin Dabov, Alessandro Foi, Vladimir Katkovnik and Karen Egiazarian, "Image denoising by sparse 3-D transform-domain collaborative filtering," IEEE Transactions on Image Processing, vol. 16, no. 8, pp2080-2095, 2007

[4] Antoni Buadès, Bartomeu Coll and Jean Michel Morel, "A non-local algorithm for image denoising," in Proceedings of the IEEE Computer Society Conference on Computer Vision and Pattern Recognition, pp60–65, 2005

[5] Hongyan Zhang, Wei He, Liangpei Zhang, Huanfeng Shen and Qiangqiang Yuan, "Hyperspectral image restoration using low-rank matrix recovery," IEEE Transactions on Geoscience and Remote Sensing, vol. 52, no. 8, pp4729-4743, 2013

[6] Yao Wang, Jiangjun Peng, Qian Zhao, Yee Leung, Xi-Le Zhao and Deyu Meng, "Hyperspectral image restoration via total variation regularized low-rank tensor decomposition," IEEE Journal of Selected Topics in Applied Earth, vol. 11, no. 4, pp1227-1243, 2017

[7] Hongyan Zhang, Wei He, Liangpei Zhang, Huanfeng Shen and Qiangqiang Yuan, "Double low-rank matrix decomposition for hyperspectral image denoising and destriping," IEEE Transactions on Geoscience and Remote Sensing, vol. 60, pp1-19, 2021

[8] Lina Zhuang, José M. Bioucas-Dias, "Fast hyperspectral image denoising and inpainting based on low-rank and sparse representations," IEEE Journal of Selected Topics in Applied Earth Observations and Remote Sensing, vol. 11, no. 3, pp730-742, 2018

[9] Lina Zhuang, Xiyou Fu, Michael K. Ng and José M. Bioucas-Dias, "Hyperspectral image denoising based on global and nonlocal low-rank factorizations," IEEE Transactions on Geoscience and Remote Sensing, vol. 59, no. 12, pp10438-10454, 2021

[10] Fan Fan, Yong Ma, Chang Li, Xiaoguang Mei, Jun Huang and Jiayi Ma, "Hyperspectral image denoising with superpixel segmentation and low-rank representation," Information Sciences, vol. 397, pp48-68, 2017

[11] Minghua Zhang, Xuan Wu, Wei Song, Haibin Mei, Qi He and Cheng Su, "Hyperspectral image denoising based on superpixel block clustering and low-rank characteristics (in Chinese)," Journal of Data Acquisition and Processing, vol. 38, pp549-564, 2023

[12] Yu-Bang Zheng, Ting-Zhu Huang, Xi-Le Zhao, Yong Chen and Wei He, "Double-factor regularized low-rank tensor factorization for mixed noise removal in hyperspectral image," IEEE Transactions on Geoscience and Remote Sensing, vol. 58, no. 12, pp8450–8464, 2020

[13] Orhan Torun, Seniha Esen Yuksel, Erkut Erdem, Nevrez Imamoglu and Aykut Erdem, "Hyperspectral image denoising via self-modulating convolutional neural networks," Signal Processing, vol. 214, 2024

[14] Wei Hu, Jiahao Pang, Xianming Liu, Dong Tian, Chia-Wen Lin and Anthony Vetro, "Graph signal processing for geometric data and beyond: Theory and applications," IEEE Transactions on Multimedia, vol. 24, pp3961-3977, 2021

[15] Xiaoqiang Lu, Yulong Wang and Yuan Yuan, "Graph-regularized low-rank representation for destriping of hyperspectral images," IEEE Transactions on Geoscience and Remote Sensing, vol. 51, no. 7, pp4009-4018, 2013

[16] Du-Yih Tsai, Yongbum Lee and Eri Matsuyama, "Information entropy measure for evaluation of image quality," Journal of Digital Imaging, vol. 21, pp338-347, 2008

[17] Radhakrishna Achanta, Appu Shaji, Kevin Smith, Aurelien Lucchi, Pascal Fua and Sabine Süsstrunk, "SLIC superpixels compared to state-of-the-art superpixel methods," IEEE Transaction Pattern Analysis Machine Intelligence, vol. 34, no. 11, pp2274–2282, 2012

[18] David I Shuman, Sunil K. Narang, Pascal Frossard, Antonio Ortega and Pierre Vandergheynst, "The emerging field of signal processing on graphs: Extending high-dimensional data analysis to networks and other irregular domains," IEEE Signal Processing Magazine (1991-present), vol. 30, no. 3, pp83-98, 2013

[19] Lan Li, Shang Bao, Mingli Jing and Dan Wang, "Hyperspectral image denoising using superpixel segmentation and graph Laplacian regularization," IEEE Geoscience and Remote Sensing Letters, vol. 21, pp1-5, 2024

[20] Matteo Maggioni, Vladimir Katkovnik, Karen Egiazarian and Alessandro Foi, "Nonlocal transform-domain filter for volumetric data denoising and reconstruction," IEEE Transaction Image Processing, vol. 22, no. 1, pp119–133, 2013

[21] Xin Su, Zhi Zhang and Fang Yang, "Fast hyperspectral image denoising and destriping method based on graph Laplacian regularization," IEEE Transactions on Geoscience and Remote Sensing, vol. 61, pp1-14, 2023